APPLIED OPTICS

Self-assembly of highly efficient, broadband plasmonic absorbers for solar steam generation

Lin Zhou,[1]***** **Yingling Tan,**[1]***** **Dengxin Ji,**[2] **Bin Zhu,**[1] **Pei Zhang,**[3] **Jun Xu,**[3] **Qiaoqiang Gan,**[2] **Zongfu Yu,**[4] **Jia Zhu**[1]†

The study of ideal absorbers, which can efficiently absorb light over a broad range of wavelengths, is of fundamental importance, as well as critical for many applications from solar steam generation and thermophotovoltaics to light/thermal detectors. As a result of recent advances in plasmonics, plasmonic absorbers have attracted a lot of attention. However, the performance and scalability of these absorbers, predominantly fabricated by the top-down approach, need to be further improved to enable widespread applications. We report a plasmonic absorber which can enable an average measured absorbance of ~99% across the wavelengths from 400 nm to 10 μm, the most efficient and broadband plasmonic absorber reported to date. The absorber is fabricated through self-assembly of metallic nanoparticles onto a nanoporous template by a one-step deposition process. Because of its efficient light absorption, strong field enhancement, and porous structures, which together enable not only efficient solar absorption but also significant local heating and continuous stream flow, plasmonic absorber–based solar steam generation has over 90% efficiency under solar irradiation of only 4-sun intensity (4 kW m^{-2}). The pronounced light absorption effect coupled with the high-throughput self-assembly process could lead toward large-scale manufacturing of other nanophotonic structures and devices.

INTRODUCTION

For a wide range of applications from photo/thermal detections (1–6) and solar energy conversion (7–13) to infrared imaging (14), the efficiency and bandwidth of absorbers will ultimately limit the performance of the whole system. An ideal absorber should eliminate transmittance and reflectance over a broad spectral range. Therefore, there are generally three critical elements in the design of ideal absorbers: efficient antireflection (15, 16), high density of optical modes (10, 17), and strong light coupling for efficient absorption. Previously, various plasmonic nanostructures, such as metallic meta-atoms (meta-surfaces) or tapered geometries have been heavily investigated to broaden the absorption bandwidth by constructing multiple resonances (18–24). For example, a plasmonic absorber based on a crossed trapezoid grating array reported by Aydin et al. (19) achieved a measured absorption of 0.71 over a spectral range of 400 to 700 nm. An absorptive meta-absorber achieved by ultra sharp convex metal grooves was reported by Søndergaard et al. (20), which experimentally demonstrated an average absorbance of 96% over 450 to 850 nm. Refractory materials, for example titanium nitride or vanadium dioxide, are also used as alternatives to construct the plasmonic absorber (25, 26). However, there are several limitations that can hinder the use of these absorbers for widespread applications. First, the structures of absorbers are fabricated predominantly by top-down lithography such as focused ion beam (FIB) and e-beam lithography (EBL), with inherent limitations on fabrication throughput, spatial resolution, and scalability. Second, in all of these previous studies the light absorption is enabled by a very limited number of well defined resonant nanostructures which are compact-aggregated on bulk optical substrates; thus the efficiency and bandwidth of these absorbers need to be further improved.

There are two key components in our structures, working together to achieve highly efficient and broadband absorption (Fig. 1A). Gold nanoparticles with random sizes and distributions enable a high density of hybridized localized surface plasmon resonance (LSPR) to effectively absorb light in a wide wavelength range; nanoporous templates (porosity, ≳40%) provide an impedance match for efficient reflection reduction and coupling to the optical modes. Therefore, this structure can enable an average measured light absorbance of ~99% throughout the visible to mid-infrared regimes (400 nm to 10 μm). As far as we know, it is the most efficient and broadband plasmonic absorber reported to date.

Significant progress has been made in the field of self-assembly, with various methods that have been developed with wonderful control of uniformity and directionality through molecular interactions, external directing fields, etc. (27–33). Compared with the top-down method (such as EBL, FIB, etc.), self-assembled processes offer several advantages, such as high spatial resolution (1- to 2-nm interparticle distance) and efficient scale-up, as well as high throughput.

RESULTS

For the applications of an efficient and broadband plasmonic absorber, it is desirable to assemble random-sized, widely anisotropic-shaped gold nanoparticles in a close-packed (but not aggregated) fashion, which is not feasible with the conventional bottom-up approach. Therefore, we developed a template-assisted physical vapor deposition (PVD) process (see Supplementary Materials and note S1 for details). A schematic outline of the plasmonic absorber formation (a "unit cell") is shown in Fig. 1B. A nanoporous alumina template was used to form a percolated scaffold for hosting gold nanoparticles (34); these templates were fabricated using a two-step anodization process that enabled the pore size

[1]National Laboratory of Solid State Microstructures, College of Engineering and Applied Sciences, and Collaborative Innovation Center of Advanced Microstructures, Nanjing University, Nanjing 210093, China. [2]Department of Electrical Engineering, University at Buffalo, The State University of New York, Buffalo, NY 14260, USA. [3]School of Electronic Science and Engineering, Nanjing University, Nanjing 210093, China. [4]Department of Electrical and Computer Engineering, University of Wisconsin Madison, Madison, WI 53706, USA.
*These authors contributed equally to this work.
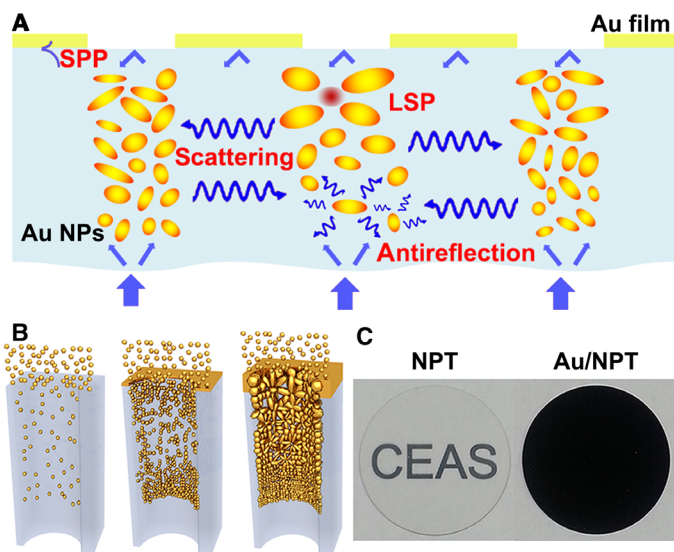†Corresponding author. E-mail: jiazhu@nju.edu.cn

Fig. 1. Schematic, processes, and photographs of plasmonic absorbers. (**A**) Schematic of an ideal plasmonic absorber. (**B**) Self-assembly of gold nanoparticles on nanoporous templates to form plasmonic absorbers. (**C**) Digital camera images of a 1-inch-diameter bare nanoporous template sample and a ≲90-nm-thick Au/NPT sample (observed from the template side). CEAS, College of Engineering and Applied Sciences.

to be finely controlled in the range of 30 to 400 nm. The orders and periodicity of these nanopores can also be controlled through a variety of techniques (35–37).

These nanoporous templates were then transferred to a PVD system (Gatan, model 682) for the self-assembly deposition of gold nanoparticles. At low gas pressures (≲1×10^{-3} Pa), the gold ions fly ballistically from the target in straight lines and travel deep (~1 μm) into the pores. They energetically affect the sidewall of each pore in the template. At higher gas pressures (≳1 Pa), gold ions collide with the gas atoms that act as a moderator and move diffusively, reaching the top surface and sidewall and condensing after undergoing a random walk. Therefore, by finely tuning the pore size of the nanoporous templates and the gas pressure of the PVD system, gold nanoparticles of different sizes can be deposited on both the top surface and sidewalls of the pores in the templates (35). During the process of deposition, the deposited gold on the surface (rather than sidewall) forms a metallic film. Meanwhile, nanoparticles down in the pores adhere to the walls and aggregate, forming a randomly distributed profile. Because metal nanoparticles are more likely to gather near the entrance of a pore, the sizes of nanoparticles change gradually along the deposition path. As shown in Fig. 1B, the particles near the top surface (deposited gold film side) are larger and sparser, whereas those down in the pore are smaller and more densely packed. As explained later, the random distribution of particles with different sizes and shapes plays a critical role in enabling efficient and broadband plasmonic absorption. Figure 1C compares an optical photograph of a 1-inch-diameter bare nanoporous template (which is transparent) with that of a ≲90-nm-thick gold-deposited nanoporous template (labeled as Au/NPT; black).

A three-dimensional (3D) schematic of the ideal plasmonic absorber is presented in Fig. 2A, which consists of a perforated gold film, randomly distributed gold nanoparticles, and a nanoporous template
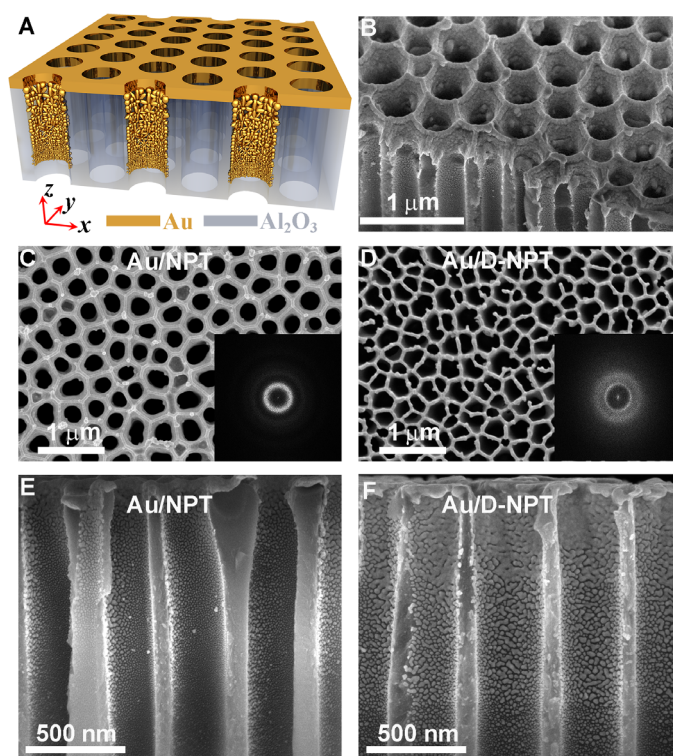

Fig. 2. Structures of self-assembled plasmonic absorbers. (**A**) 3D schematic of self-assembled plasmonic absorbers. (**B**) 3D SEM image of a typical Au/NPT sample. (**C** and **E**) Top view (C) and cross-sectional (E) SEM images of Au/NPT sample. The geometry parameters of the Au/NPT sample are the average pore size D ~300 nm and effective gold film thickness ~60 nm. (**D** and **F**) Top-view (D) and cross-sectional (F) SEM images of the Au/D-NPT sample with the average pore size D ~365 nm and effective gold film thickness ~85 nm. The insets in (C) and (D) are the corresponding Fourier transform diagrams of Au/NPT and Au/D-NPT, respectively.

(an average pore diameter D of ~300 nm and a pore-to-pore distance L of 450 nm). Figure 2B presents a typical high-resolution scanning electron microscopy (SEM) image of our self-assembled plasmonic absorber. Note that pore diameter D is the most critical of all the geometry parameters (see Supplementary Materials, note S2, and figs. S1 to S3 for details) and random gold nanoparticles are the most critical component responsible for the broadband plasmonic absorption effect. Large pore diameter will allow the formation of close-packed gold nanoparticles with a variety of aspect ratios during the PVD (Fig. 2, E and F), therefore increasing the density of plasmonic resonant modes. In addition, large pore–sized porous templates with a much reduced refractive index and small impedance mismatch (see Supplementary Materials, note S3, and figs. S4 and S5 for details) will enable extremely low reflectance and efficient light coupling within these pores, therefore significantly enhancing the absorption. In the experiment, absorbers with various pore diameters were fabricated and characterized systematically. The corresponding top view and cross-sectional SEM images of Au/NPT (D = 300 nm), acquired using dual-beam FIB microscopy (Dual Beam FIB 235, FEI Strata), are shown in Fig. 2 (C and E, respectively). The corresponding SEM images of an absorber with larger pores and a more disordered nanoporous template (noted as Au/D-NPT; D = 365 nm; see Materials and Methods) are presented in Fig. 2 (D and F). As

indicated in the corresponding inset diagrams, the distribution of the Fourier transform image of the Au/D-NPT sample is much more diffusive. It is expected that the disorder of pore arrays in Au/D-NPT gives rise to more favorable light coupling and excitations of high density of surface plasmon polariton (SPP) modes, leading to the pronounced plasmonic absorption enhancement by effectively coupling with the LSPR of gold particles.

To quantitatively characterize the performance of the absorber, the absorption spectra of three samples (the bare nanoporous template and two gold-sputtered templates Au/NPT and Au/D-NPT) were first measured over a wavelength range of 400 nm to 10 μm (Fig. 3, A and B). In the visible–near-infrared regime (400 nm to 2.5 μm), the absorption spectra were measured using an ultraviolet–visible–near-infrared spectrophotometer with an integrated sphere attachment (see Materials and Methods). As shown in Fig. 3A, the average measured absorbance increases to ~99% for the Au/D-NPT sample (~90% for the Au/NPT sample). In the mid-infrared regime (2.5 to 10 μm) (Fig. 3B), the absorption spectra were measured using Fourier transform infrared (FTIR) spectroscopy (see Materials and Methods). It is clearly observed that the absorbance of the bare alumina nanoporous template (red line in

Fig. 3B) experiences a slight absorption peak around λ = 3 μm (~25%) and increases distinctly for λ > 6 μm (~23% at λ = 6 μm), which can be attributed to the intrinsic infrared absorption of alumina and leads to the high absorption performance in the range λ > 8 μm. After a ~60-nm-thick gold deposition on the nanoporous template with a porosity of ~38%, the absorption efficiency of the Au/NPT absorber was efficiently enhanced by gold, with a minimal absorbance up to >40%. More strikingly, the minimal absorbance of the Au/D-NPT (thick black line in Fig. 3B) was raised up to 98.6% and an average of absorbance reached >99% over the mid-infrared spectrum.

The full-wave electromagnetic simulations were carried out using the FDTD to explore the physical mechanism for the plasmonic absorber. In the structure modeling, the distribution profiles of the metallic nanoparticles on the surface and inside the pores of nanoporous templates were modeled on the basis of the SEM images in Fig. 2 (see Materials and Methods for details). The calculated absorption curves of the Au/NPT absorber (black solid line) and bare nanoporous template (red solid line) are shown in Fig. 3 (C and D) for λ = 400 nm to 10 μm. One may find that the typical absorption features of the Au/NPT absorber observed in the experiment are reproduced well by our
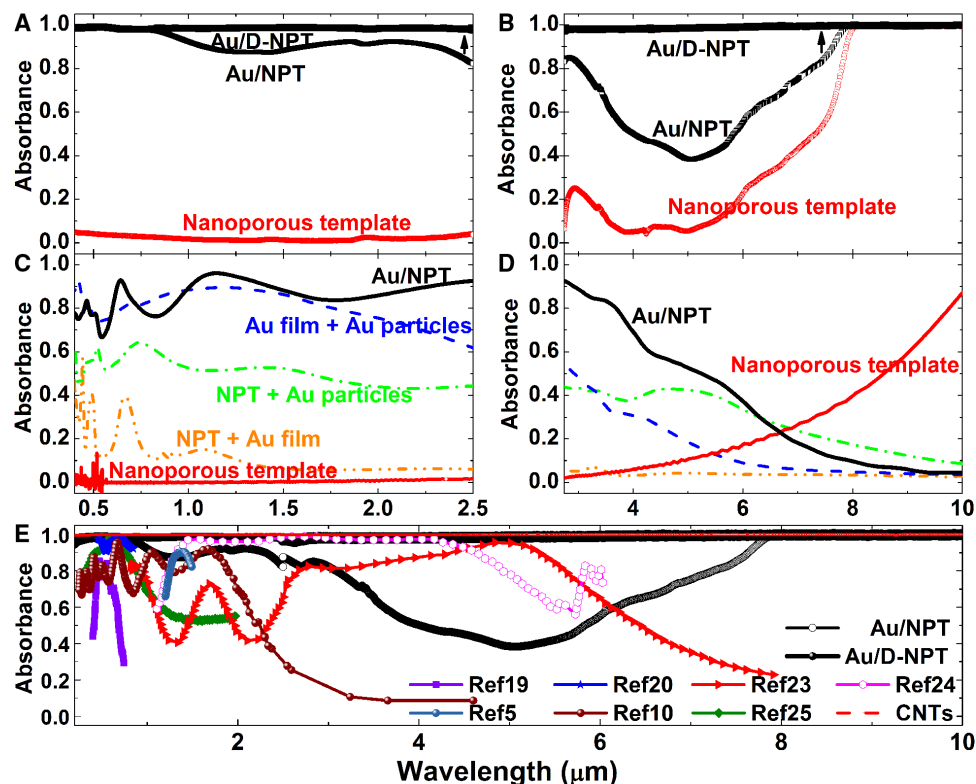

Fig. 3. Broadband absorption properties of the self-assembled plasmonic absorbers. (**A**) Experimental absorption spectra measured by an integrated sphere in the visible and near-infrared regimes. (**B**) Experimental absorption spectra measured by specular reflectance in the mid-infrared regime. The thin red, thin black, and thick black lines in (A) and (B) represent the bare nanoporous templates Au/NPT and Au/D-NPT samples, respectively. (**C** and **D**) Finite-difference time-domain (FDTD) method–calculated absorption spectra of the bare nanoporous template (red solid line) and Au/NPT (black solid line) samples. The other dashed lines in (C) and (D) represent simulated absorption curves of three virtual geometries, that is, the nanoporous template with gold perforated film (orange), the nanoporous template with gold nanoparticles (green), and the perforated gold film with nanoparticles (blue), respectively. (**E**) Comparisons of absorption performance between our plasmonic absorbers (black solid line for Au/D-NPT and black hollow line for Au/NPT, respectively) and other reported structures (other colored dashed lines). The absorbance curve of a standard carbon nanotube sample on a silicon substrate was shown by the red dashed line as well. The other colored lines are absorption curves subtracted from the related references, respectively. CNT, carbon nanotube.

simulations over the visible-infrared regime (especially for λ = 400 nm to 6 μm), indicating that the essential mechanisms of the absorption are grasped well by our simulation model.

To elucidate how the three individual parts of the plasmonic absorber work, the absorption spectra of (i) the nanoporous template with the gold perforated film, (ii) the nanoporous template with gold nanoparticles, and (iii) the gold perforated film with gold nanoparticles were calculated individually, as ticked by the orange, green, and blue dashed lines in Fig. 3 (C and D), respectively. In the visible–near-infrared regime (400 nm to 2.5 μm), the calculated curve of the Au/NPT structure is broadband absorptive with an average absorbance of ~82%. Comparisons between absorption curves of Au/NPT and "the nanoporous template with the gold perforated film" reveal that gold nanoparticles inside pores are the main absorption carriers. Because gold nanoparticles are closely packed in random distributions along the z direction (Fig. 2E), the LSPR of each gold nanoparticle will overlap and hybridize, leading to multiple overlapping plasmonic modes that give rise to broadband absorption (10). Comparisons between absorption curves of Au/NPT and "the nanoporous template with gold nanoparticles" reveal that the gold film plays an important role in enhancing the overall absorption, especially in the visible and near-infrared range. Although the gold film is weakly absorptive, especially in the infrared range (orange line in Fig. 3, C and D), because gold particles sputtered on the surface are connected and form a patterned film (Fig. 2B), such a gold film can effectively reflect light back to the absorber and significantly increase the optical path length of absorption in gold particles. Furthermore, the transverse periodicity of gold film can provide effective light coupling to the SPP excitations. Because the nanopores are assumed to be perfectly ordered in the model, the simulated curve of Au/NPT (thin black line in Fig. 3C) is of discrete peaks (rather than flat measured profile in Fig. 3A), and the overall simulated absorbance is lower than the experimental one (38). Because both SPP and LSPR play roles in absorption, it is expected that the bandwidth and cutoff absorption frequency of absorbers can be finely tuned by the metallic particles and pore size of nanoporous templates. This is important for many applications such as thermophotovoltaics (39, 40).

As shown in Fig. 3D, in the mid-infrared regime (λ = 2.5 to 6 μm), there is a large difference (~40%) between absorption curves of Au/NPT and "the gold perforated film with gold nanoparticles," which indicates the important role of the nanoporous templates. Without the nanoporous template, the absorbance caused by overlapping of LSPR and SPP modes decreases distinctly, especially for λ > 2 μm. The nanoporous template with large porosity (≳40%) provides strong scattering and internal reflection so that optical path lengths are significantly increased (41). In addition, the template with large porosity can exhibit strong antireflective properties due to the relative low effective index, which further boosts the absorption efficiency (42) (see Supplementary Materials and note S3). For λ = 6 to 10 μm, the simulated absorbance of Au/NPT is much lower than the experimental absorbance due to the underestimation of the intrinsic absorbance (red dashed line in Fig. 3D) of nanoporous template. In the experiment, an approximately 50-μm-thick template is used, whereas in the simulation, limited by calculation resources, a 500-nm-thick section is selected, therefore causing the underestimation of absorption in this range (see Supplementary Materials, note S4, and figs. S6 to S8).

On the basis of the above analysis, the excellent performance of Au/D-NPT (Fig. 3, A and B) can be attributed to several factors. First,

the Au/D-NPT absorber with larger pore diameter D is more favorable for the formation during the PVD of close-packed gold nanoparticles with a wide variety of aspect ratios. This increases the density of plasmonic resonant modes, which is critical for broadband absorptions. Second, because the porosity of the Au/D-NPT sample (~59%) is much larger than that of the Au/NPT sample (~38%), reduced reflection, higher density of LSPR modes, and a stronger scattering effect can be expected. Third, the transverse pattern of the Au/D-NPT sample is more disordered than that of the Au/NPT sample (Fig. 2, C and D), and higher density of SPP modes can be excited in the visible and near-infrared regime. Therefore, our Au/D-NPT sample is suggested to be the most efficient and broadband plasmonic absorber (average absorbance of ~99% over 200 nm to 10 μm) among the various plasmonic absorbers reported to date. It is also comparable to the carbon nanotube–based absorber within this range, as demonstrated in Fig. 3E.

Our plasmonic absorbers can be used directly for efficient solar steam generation (8, 43, 44) because of the highly efficient, broadband absorption. As outlined in Fig. 4A, our plasmonic absorber shows several unique features. First, the light absorption is efficient (above 99%) across the full solar spectrum. Second, the gold particles are very close-packed with very strong field enhancement around the metal/water interface in a wide range of spectrum, leading to strong nonradiative plasmon decay, which is beneficial for efficient solar steam generation. Figure 4B gives four calculated cross-sectional electric field distributions at four arbitrary wavelengths, indicating the widely spread hot spots of our plasmonic structure. Third, because of the unique porous nature of templates, the absorber samples float naturally on the top surface of water, with gold particles in direct contact with the water surface. The direct and straight pores provide convenient paths for continuous steam flow. In the experiment (see Materials and Methods for details of the experiments), solar irradiations of different power densities (up to 13 kW m^{-2}) are obtained from a solar simulator (Newport 94043A) combined with a double-lens system, and then projected on the surface of samples. With the solar simulator on, plenty of nucleation sites for steam generation are formed on the surface of samples. After an initial transient period, massive bubbles continuously generate and leave the water surface, indicating the steady steam generations. Optical images of samples with the solar irradiations off/on are shown in Fig. 4C. The typical experimental comparisons of time-dependent mass change due to steam generation under different solar irradiations were provided in Fig. 4D. It is expected that the evaporation rate will be accelerated with the increased illumination intensity. Subtracting the evaporation rate from the slope of mass loss curve in Fig. 4D, it is obvious that evaporation rates with our plasmonic absorbers are 2.1 and 3.6 times of pure water at 1 and 4 kW m^{-2} solar irradiations, respectively. Such an evaporation enhancement effect is easily repeatable and more pronounced under higher solar irradiation. On the basis of more than four sets of independent experimental measurements for each illumination intensity, the average evaporation rate as well as the SD are shown in Fig. 4E. Accompanied by an almost linear increment of evaporation rate, the temperature of the generated steam increases steadily, approaching ~98°C (for open measurement) and ~110°C (for closed measurement) under >8 kW m^{-2} solar irradiation. To evaluate the solar steam efficiency η in the solar-to-thermal conversion process, we used η = $\dot{m}h_{LV}/P_{in}$, in which $\dot{m}$ is the mass flux, h_{LV} is the liquid-vapor phase change enthalpy, and P_{in} is the received power density of the solar irradiations on the absorber surface (7). One may find from Fig. 4E that, under a solar irradiation of only 4 kW m^{-2}, the efficiency of
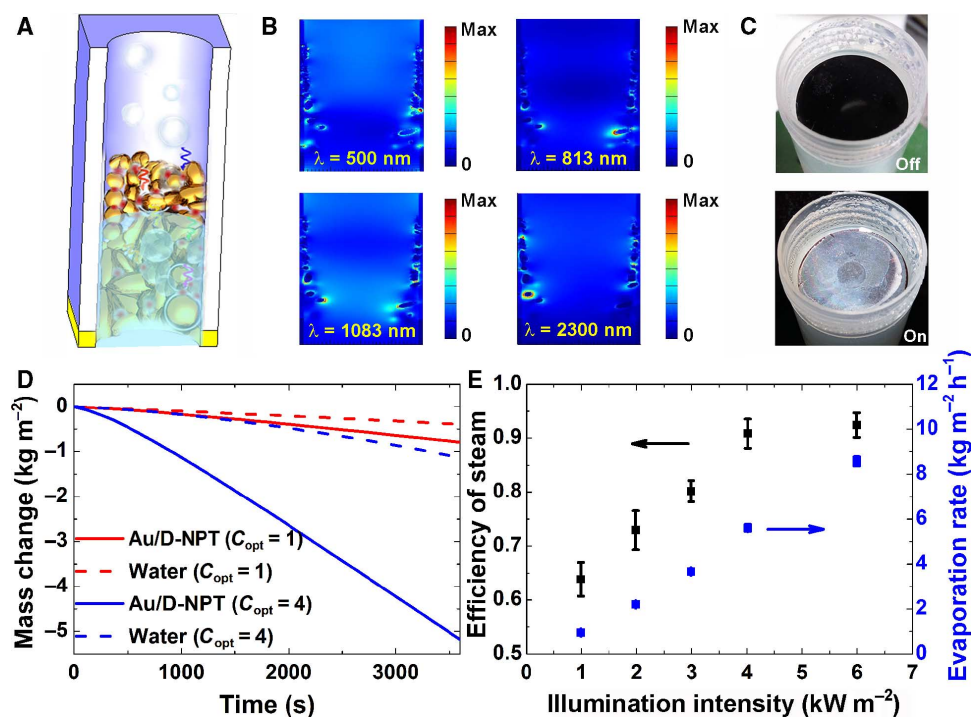
Fig. 4. Plasmonic absorbers for solar steam generation. (**A**) Schematic of the solar steam experiment. (**B**) Calculated cross-sectional electric field distributions at four arbitrary wavelengths. (**C**) Experimental setups for solar steam generation with the solar simulator off (upper) and on (lower). (**D**) Evaporation mass change of water with (solid lines) and without (dashed lines) the plasmonic absorbers (Au/D-NPT) as a function of time under different solar irradiations: 1 kW m^{-2} (red line) and 4 kW m^{-2} (blue line). (**E**) Solar steam efficiency (black, left-hand side axis) and evaporation rate (blue, right-hand side axis) with plasmonic absorbers as a function of illumination intensity on the absorber surface.

solar steam generation assisted by our plasmonic structure was up to 90%. Such a nonlinear increment of evaporation rate and efficiency is related to the nonlinear variation of thermal motion or steam temperature on P_{in} (see note S5 and fig. S9 for details). Apart from the plasmonic hot-spot effect that is favorable for local heating, we stress that the radiation loss (45, 46) of our absorber is low (the estimated maximal loss is ~3% at 4 sun illumination; see Supplementary Materials, note S6, and fig. S10 for more details). The efficient solar-to-steam conversion efficiency mainly originated from the characteristics of our developed plasmonic absorber: broadband and highly efficient absorption effect, plasmonic hot spot–enabled local heating, and the inherent multiple nanopore structures. Compared to steam generation used in traditional concentrated solar power systems, where high concentration and high temperature are necessary to drive steam turbines, this type of plasmonic absorber–based steam generation with local surface heating and relatively low temperature is particularly favorable for applications such as solar desalination and sterilization.

DISCUSSION

In summary, we report a highly efficient (~99%), broadband (200 nm to 10 μm) plasmonic light absorber that operates over the visible-infrared regime. The pronounced absorption effects are attributed to the high density of optical modes, strong multiple scattering (or internal reflection), and low effective refractive index offered by the nanoporous templates and metallic nanoparticles, which show distinct advantages over the traditional multiplexed plasmonic nanostructures and/or the carbon

black–based absorbers (see note S7 and figs. S11 and S12 for details). This type of plasmonic absorber can be directly used for efficient solar steam generation (over 90% conversion efficiency at 4 kW m^{-2} solar irradiations). With more advancement in the design and fabrication of different templates (47) and nanoparticles, we expect that the self-assembly approach (48), together with low-cost plasmonic materials such as aluminum, will open up exciting new scalable and high-throughput processing schemes which will facilitate the large-scale manufacture of complex nanoscale architectures; this will also make an impact in a diverse set of other potential application fields, such as desalination, solar thermophotovoltaics, photocatalysis, metamaterials, and sensing technology.

MATERIALS AND METHODS

Fabrications and optical measurements

The broadband absorptive metallic nanostructures were prepared by the PVD of gold deposition on different pore–sized alumina nanoporous templates. The nanoporous template was fabricated by a two-step anodization method and then sputtered with gold nanoparticles by a PVD system (Gatan, model 682). The pore radius and porosity were controlled by the voltage and oxidation time. The sparsely distributed profiles of the nanoparticles were controlled by the deposition time and degree of vacuum. During a systematic optimization procedure with different sizes and distributions of nanopores, the Au/D-NPT (Au/NPT) absorber was fabricated with gold sputtered (an effective thickness of ~60 to 85 nm) on the more (or less) disordered nanoporous template, respectively. The parameters were as follows: average pore

diameter D ~365 nm (D ~300 nm), higher porosity f ~59% (f ~38%), and pore-to-pore distance L ~450 nm. Optical transmittance and reflectance measurements on the metallic absorbers were carried out using different optical measurement systems. A Shimadzu UV-3600 (UV-Vis-NIR) spectrophotometer attached with an integrating sphere (ISR-3100) was used for the hemispherical reflectance measurements in the UV-Vis-NIR range (200 nm to 2.5 μm) (Fig. 3A). A PerkinElmer GX FTIR spectroscope with specular transmittance and reflectance accessories was used for the mid-infrared regime (400 to 4000 cm^{-1}) (Fig. 3B), which has a resolution of 4 cm^{-1}. The measured mid-infrared absorbance of the Au/NPT absorber was repeated by the Nicolet 6700 FTIR spectroscope with diffusive reflectance accessories.

Optical modeling and simulation

Full-wave electromagnetic simulations were carried out using the FDTD method based on FDTD Solutions 8.6.1 software by Lumerical. In the optical modeling, hexagonal periodic structure was used, which consisted of random gold nanoparticles (inside each pore), periodically perforated gold film, and alumina nanoporous template. Limited by the computational resources (the min-server used was equipped with 128 GB RAM and double CPU of 2.7 GHz), the thickness of gold nanoparticles inside the pore and bare nanoporous template substrate were assumed to be distributed only to $h_p = 400$ nm and $H = 500$ nm in the Au/NPT simulation. To reproduce the most representative distribution profile of the nanoparticles in the SEM image (Fig. 2B), the randomly distributed ellipsoid nanoparticles with graded long axis length were considered. The maximal (minimal) long axis length of the random nanoparticles was set at 100 nm (10 nm), whereas the short axis length was fixed at 20 nm. Therefore, the aspect ratio of the nanoparticle could be tuned by the long axis length. The density of nanoparticles along each pore was gradually increased along the pore axis (according to the cross-sectional SEM in Fig. 2F). For simplicity, the total length of particles ($h_p = 400$ nm) was divided into eight sections, and the particle number of each section (from gold film to nanoporous template side) was linearly increased. The total number of particles inside each pore was ~2300, with the total quantity of gold deposited into a nanopore determined by the deposition condition (see note S8 and fig. S13 for details). One physical unit cell was simulated in the FDTD simulation, with an excited plane wave propagating along the z direction and periodic boundary conditions applied in the transverse directions (Fig. 2A). Because the response of such a 3D metallic nanostructure is not sensitive to the polarization and incident angle (see note S9 and fig. S14 for details), for simplicity, the polarization of light was set along the x axis. The total transmission and reflection efficiency were then detected by two power monitors, and absorption efficiency was calculated by $A = 1 - R - T$. The permittivity of alumina and gold used in the simulation was obtained from Palik's data (49). In addition, the pore radius, pore-to-pore distance, and metal thickness for the Au/NPT simulation, as well as the thickness of alumina for the bare nanoporous template simulation, were set as the same as in the experiment.

Solar steam measurements

The experimental setup of the solar steam measurement was composed of a solar simulator (Newport 94043A), a double-lens focusing system (200-mm focal length and 100-mm diameter for lens #1; 50-mm focal length and 30-mm diameter for lens #2; Beijing Optical Century Instrument Co.), a power meter (10 W, 19-mm-diameter detector; #1097901, Coherent), a test chamber, a balance (FA2004, 0.1-mg accuracy), thermocouples, a serial communication module (RS232), and a desktop computer. The experiments were typically conducted at an ambient temperature of 24°C and humidity of ~42%.

The designed test chamber was a Dewar flask (28-mm inner diameter, 38-mm outer diameter, and 96-mm height; Shanghai Glass Instrument Co.). The temperature of the steam and water around the sample was recorded by two thermocouples (placed on top/bottom surface of the sample, respectively). All the thermocouples were coated with a highly reflective white titanium oxide coating by atomic layer deposition to suppress the heating effect of direct illumination. The illumination source was a solar simulator (Class AAA, Newport 94043A) with an optical filter for the standard air mass 1.5-G spectrum. The output solar irradiation of the solar simulator was focused by the double-lens system and projected on the surface of the sample (held by the Dewar flask). The power density of the illumination intensity was measured at the level of the sample with the power meter (air cool thermopile sensor with a 19-mm-diameter detector, PM10; #1097901, Coherent). By carefully optimizing the double-lens focusing system, the maximal irradiation power was ~13 kW m^{-2}. The balance (FA2004, 0.1-mg accuracy) was used to monitor the mass loss from evaporation, recorded in real time by the desktop computer (with RS 232 serial ports), and then used to determine the evaporation rate and efficiency of solar steam generation.

REFERENCES AND NOTES

1. Z.-P. Yang, L. Ci, J. A. Bur, S.-Y. Lin, P. M. Ajayan, Experimental observation of an extremely dark material made by a low-density nanotube array. *Nano Lett.* **8**, 446–451 (2008).
2. K. Mizuno, J. Ishii, H. Kishida, Y. Hayamizu, S. Yasuda, D. N. Futaba, M. Yumura, K. Hata, A black body absorber from vertically aligned single-walled carbon nanotubes. *Proc. Natl. Acad. Sci. U.S.A.* **106**, 6044–6047 (2009).

3. J. Lehman, A. Sanders, L. Hanssen, B. Wilthan, J. Zeng, C. Jensen, Very black infrared detector from vertically aligned carbon nanotubes and electric-field poling of lithium tantalate. *Nano Lett.* **10**, 3261–3266 (2010).

4. X. He, N. Fujimura, J. M. Lloyd, K. J. Erickson, A. A. Talin, Q. Zhang, W. Gao, Q. Jiang, Y. Kawano, R. H. Hauge, F. Léonard, J. Kono, Carbon nanotube terahertz detector. *Nano Lett.* **14**, 3953–3958 (2014).

5. W. Li, J. Valentine, Metamaterial perfect absorber based hot electron photodetection. *Nano Lett.* **14**, 3510–3514 (2014).

6. C.-H. Liu, Y.-C. Chang, T. B. Norris, Z. Zhong, Graphene photodetectors with ultra-broadband and high responsivity at room temperature. *Nat. Nanotechnol.* **9**, 273–278 (2014).

7. H. Ghasemi, G. Ni, A. M. Marconnet, J. Loomis, S. Yerci, N. Miljkovic, G. Chen, Solar steam generation by heat localization. *Nat. Commun.* **5**, 4449 (2014).

8. O. Neumann, C. Feronti, A. D. Neumann, A. Dong, K. Schell, B. Lu, E. Kim, M. Quinn, S. Thompson, N. Grady, P. Nordlander, M. Oden, N. J. Halas, Compact solar autoclave based on steam generation using broadband light-harvesting nanoparticles. *Proc. Natl. Acad. Sci. U.S.A.* **110**, 11677–11681 (2013).

9. A. Lenert, D. M. Bierman, Y. Nam, W. R. Chan, I. Celanović, M. Soljačić, E. N. Wang, A nanophotonic solar thermophotovoltaic device. *Nat. Nanotechnol.* **9**, 126–130 (2014).

10. J. B. Chou, Y. X. Yeng, Y. E. Lee, A. Lenert, V. Rinnerbauer, I. Celanovic, M. Soljačić, N. X. Fang, E. N. Wang, S.-G. Kim, Enabling ideal selective solar absorption with 2D metallic dielectric photonic crystals. *Adv. Mater.* **26**, 8041–8045 (2014).

11. J.-H. Lee, Y.-S. Kim, K. Constant, K.-M. Ho, Woodpile metallic photonic crystals fabricated by using soft lithography for tailored thermal emission. *Adv. Mater.* **19**, 791–794 (2007).

12. K. A. Arpin, M. D. Losego, A. N. Cloud, H. Ning, J. Mallek, N. P. Sergeant, L. Zhu, Z. Yu, B. Kalanyan, G. N. Parsons, G. S. Girolami, J. R. Abelson, S. Fan, P. V. Braun, Three-dimensional self-assembled photonic crystals with high temperature stability for thermal emission modification. *Nat. Commun.* **4**, 2630 (2013).

13. J. Zhu, Z. Yu, G. F. Burkhard, C.-M. Hsu, S. T. Connor, Y. Xu, Q. Wang, M. McGehee, S. Fan, Y. Cui, Optical absorption enhancement in amorphous silicon nanowire and nanocone arrays. *Nano Lett.* **9**, 279–282 (2009).

14. J. P. Mailoa, A. J. Akey, C. B. Simmons, D. Hutchinson, J. Mathews, J. T. Sullivan, D. Recht, M. T. Winkler, J. S. Williams, J. M. Warrender, P. D. Persans, M. J. Aziz, T. Buonassisi, Room-temperature sub-band gap optoelectronic response of hyperdoped silicon. *Nat. Commun.* **5**, 3011 (2014).

15. F. J. García-Vidal, J. M. Pitarke, J. B. Pendry, Effective medium theory of the optical properties of aligned carbon nanotubes. *Phys. Rev. Lett.* **78**, 4289–4292 (1997).

16. J.-Q. Xi, M. F. Schubert, J. K. Kim, E. F. Schubert, M. Chen, S.-Y. Lin, W. Liu, J. A. Smart, Optical thin-film materials with low refractive index for broadband elimination of Fresnel reflection. *Nat. Photonics* **1**, 176–179 (2007).

17. Z. Yu, A. Raman, S. Fan, Fundamental limit of nanophotonic light trapping in solar cells. *Proc. Natl. Acad. Sci. U.S.A.* **107**, 17491–17496 (2010).

18. N. I. Landy, S. Sajuyigbe, J. J. Mock, D. R. Smith, W. J. Padilla, Perfect metamaterial absorber. *Phys. Rev. Lett.* **100**, 207402 (2008).

19. K. Aydin, V. E. Ferry, R. M. Briggs, H. A. Atwater, Broadband polarization-independent resonant light absorption using ultrathin plasmonic super absorbers. *Nat. Commun.* **2**, 517 (2011).

20. T. Søndergaard, S. M. Novikov, T. Holmgaard, R. L. Eriksen, J. Beermann, Z. Han, K. Pedersen, S. I. Bozhevolnyi, Plasmonic black gold by adiabatic nanofocusing and absorption of light in ultra-sharp convex grooves. *Nat. Commun.* **3**, 969 (2012).

21. Y. Cui, K. H. Fung, J. Xu, H. Ma, Y. Jin, S. He, N. X. Fang, Ultrabroadband light absorption by a sawtooth anisotropic metamaterial slab. *Nano Lett.* **12**, 1443–1447 (2012).

22. X. Xiong, S.-C. Jiang, Y.-H. Hu, R.-W. Peng, M. Wang, Structured metal film as a perfect absorber. *Adv. Mater.* **25**, 3994–4000 (2013).

23. J. Zhou, X. F. Kaplan, L. Chen, L. J. Guo, Experiment and theory of the broadband absorption by a tapered hyperbolic metamaterial array. *ACS Photonics* **1**, 618–624 (2014).

24. J. A. Bossard, L. Lin, S. Yun, L. Liu, D. H. Werner, T. S. Mayer, Near-ideal optical metamaterial absorbers with super-octave bandwidth. *ACS Nano* **8**, 1517–1524 (2014).

25. W. Li, U. Guler, N. Kinsey, G. V. Naik, A. Boltasseva, J. Guan, V. M. Shalaev, A. V. Kildishev, Refractory plasmonics with titanium nitride: Broadband metamaterial absorber. *Adv. Mater.* **26**, 7959–7965 (2014).

26. M. A. Kats, D. Sharma, J. Lin, P. Genevet, R. Blanchard, Z. Yang, M. M. Qazilbash, D. N. Basov, S. Ramanathan, F. Capasso, Ultra-thin perfect absorber employing a tunable phase change material. *Appl. Phys. Lett.* **101**, 221101 (2012).

27. J. Yeom, B. Yeom, H. Chan, K. W. Smith, S. Dominguez-Medina, J. H. Bahng, G. Zhao, W.-S. Chang, S.-J. Chang, A. Chuvilin, D. Melnikau, A. L. Rogach, P. Zhang, S. Link, P. Král, N. A. Kotov, Chiral templating of self-assembling nanostructures by circularly polarized light. *Nat. Mater.* **14**, 66–72 (2015).

28. S. Yang, X. Ni, X. Yin, B. Kante, P. Zhang, J. Zhu, Y. Wang, X. Zhang, Feedback-driven self-assembly of symmetry breaking optical metamaterials in solution. *Nat. Nanotechnol.* **9**, 1002–1006 (2014).

29. A. Kuzyk, R. Schreiber, H. Zhang, A. O. Govorov, T. Liedl, N. Liu, Reconfigurable 3D plasmonic metamolecules. *Nat. Mater.* **13**, 862–866 (2014).

30. A. Klinkova, R. M. Choueiri, E. Kumacheva, Self-assembled plasmonic nanostructures. *Chem. Soc. Rev.* **43**, 3976–3991 (2014).

31. S. Dutta, A. Bhaumik, K. C.-W. Wu, Hierarchically porous carbon derived from polymers and biomass: Effect of interconnected pores on energy applications. *Energy Environ. Sci.* **7**, 3574–3592 (2014).

32. Z. Nie, A. Petukhova, E. Kumacheva, Properties and emerging applications of self-assembled structures made from inorganic nanoparticles. *Nat. Nanotechnol.* **5**, 15–25 (2010).

33. M. Grzelczak, J. Vermant, E. M. Furst, L. M. Liz-Marzán, Directed self-assembly of nanoparticles. *ACS Nano* **4**, 3591–3605 (2010).

34. M. R. Gartia, A. Hsiao, A. Pokhriyal, S. Seo, G. Kulsh, B. T. Cunningham, T. C. Bond, G. L. Liu, Colorimetric plasmon resonance imaging using nano Lycurgus cup arrays. *Adv. Opt. Mater.* **1**, 68–76 (2013).

35. X. Sheng, J. Liu, I. Kozinsky, A. M. Agarwal, J. Michel, L. C. Kimerling, Design and non-lithographic fabrication of light trapping structures for thin film silicon solar cells. *Adv. Mater.* **23**, 843–847 (2011).

36. W. Lee, R. Ji, U. Gösele, K. Nielsch, Fast fabrication of long-range ordered porous alumina membranes by hard anodization. *Nat. Mater.* **5**, 741–747 (2006).

37. S. Shukla, K.-T. Kim, A. Baev, Y. K. Yoon, N. M. Litchinitser, P. N. Prasad, Fabrication and characterization of gold-polymer nanocomposite plasmonic nanoarrays in a porous alumina template. *ACS Nano* **4**, 2249–2255 (2010).

38. R. A. Pala, J. S. Q. Liu, E. S. Barnard, D. Askarov, E. C. Garnett, S. Fan, M. L. Brongersma, Optimization of non-periodic plasmonic light-trapping layers for thin-film solar cells. *Nat. Commun.* **4**, 2095 (2013).

39. A. P. Raman, M. A. Anoma, L. Zhu, E. Rephaeli, S. Fan, Passive radiative cooling below ambient air temperature under direct sunlight. *Nature* **515**, 540–544 (2014).

40. F. Cao, K. McEnaney, G. Chen, Z. Ren, A review of cermet-based spectrally selective solar absorbers. *Energy Environ. Sci.* **7**, 1615–1627 (2014).

41. K. Vynck, M. Burresi, F. Riboli, D. S. Wiersma, Photon management in two-dimensional disordered media. *Nat. Mater.* **11**, 1017–1022 (2012).

42. Y.-F. Huang, S. Chattopadhyay, Y.-J. Jen, C.-Y. Peng, T.-A. Liu, Y.-K. Hsu, C.-L. Pan, H.-C. Lo, Improved broadband and quasi-omnidirectional anti-reflection properties with biomimetic silicon nanostructures. *Nat. Nanotechnol.* **2**, 770–774 (2007).

43. O. Neumann, A. S. Urban, J. Day, S. Lal, P. Nordlander, N. J. Halas, Solar vapor generation enabled by nanoparticles. *ACS Nano* **7**, 42–49 (2013).

44. M. L. Brongersma, N. J. Halas, P. Nordlander, Plasmonic-induced hot carrier science and technology. *Nat. Nanotechnol.* **10**, 25–34 (2015).

45. M. Planck, *The Theory of Heat Radiation* (Dover Publication, Inc. New York, 1912).

46. P.-M. Robitaille, On the validity of Kirchhoff's law of thermal emission. *IEEE Trans Plasma Sci.* **31**, 1263–1267 (2003).

47. J. Martín, J. Martín-González, J. F. Fernández, O. Caballero-Calero, Ordered three-dimensional interconnected nanoarchitectures in anodic porous alumina. *Nat. Commun.* **5**, 5130 (2014).

48. C. Hägglund, G. Zeltzer, R. Ruiz, I. Thomann, H.-B.-R. Lee, M. L. Brongersma, S. F. Bent, Self-assembly based plasmonic arrays tuned by atomic layer deposition for extreme visible light absorption. *Nano Lett.* **13**, 3352–3357 (2013).

49. E. D. Palik, *Handbook of Optical Constants of Solids* (Academic Press, New York, 1985).

50. S. Wu, Z. Zhang, Y. Zhang, K. Zhang, L. Zhou, X. Zhang, Y. Zhu, Enhanced rotation of the polarization of a light beam transmitted through a silver film with an array of perforated S-shaped holes. *Phys. Rev. Lett.* **110**, 207401 (2013).

51. A. Kuzyk, R. Schreiber, Z. Fan, G. Pardatscher, E.-M. Roller, A. Högele, F. C. Simmel, A. O. Govorov, T. Liedl, DNA-based self-assembly of chiral plasmonic nanostructures with tailored optical response. *Nature*, **483**, 311–314 (2012).

52. Z. Fan, H. Razavi, J.-w Do, A. Moriwaki, O. Ergen, Y.-L. Chueh, P. W. Leu, J. C. Ho, T. Takahashi, L. A. Reichertz, S. Neale, K. Yu, M. Wu, J. W. Ager, A. Javey, Three-dimensional nanopillar-array photovoltaics on low-cost and flexible substrates. *Nat. Mater.* **8**, 648–653 (2009).

53. D. A. G. Bruggeman, Calculations of various physical constants of heterogeneous substance. Part I: Dielectric constants and conductivity of isotropic substance. *Ann. Phys. Berlin* **24**, 636–699 (1935).

54. D. R. Smith, W. J. Padilla, D. C. Vier, S. C. Nemat-Nasser, S. Schultz. Composite medium with simultaneously negative permeability and permittivity. *Phys. Rev. Lett.* **84**, 4184–4187 (2000).

55. W. Ma, Y. Wen, X. Yu, Broadband metamaterial absorber at mid-infrared using multiplexed cross resonators. *Opt. Express* **21**, 30724–30730 (2013).

56. A. Tittl, M. G. Harats, R. Walter, X. Yin, M. Schäferling, N. Liu, R. Rapaport, H. Giessen, Quantitative angle-resolved small-spot reflectance measurements on plasmonic perfect absorbers: Impedance matching and disorder effects. *ACS Nano* **8**, 10885–10892 (2014).

Zhou *et al. Sci. Adv.* 2016;2:e1501227   8 April 2016

8 of 8